Regional Studies in Marine Science 81 (2025) 103920

Contents lists available at ScienceDirect

Regional Studies in Marine Science

journal homepage: www.elsevier.com/locate/rsma

Characterizing the surface spatial distribution and variability of the San Matías Meridional Front from a geostationary satellite perspective

Matias De Oto Proschle [a,b,*], Sofía Muñoz [b], Violeta Valdeomillos [b], Juan Pablo Pisoni [c]

[a] Servicio Meteorológico Nacional (SMN) de, Argentina
[b] Departamento de Ciencias de la Atmósfera y los Océanos, Facultad de Ciencias Exactas y Naturales, Universidad de Buenos Aires (DCAO-FCEyN/UBA), Argentina
[c] Centro para el Estudio de Sistemas Marinos (CESIMAR-CONICET) and Universidad Nacional de la Patagonia San Juan Bosco (UNPSJB), Puerto Madryn, Chubut, Argentina

ARTICLE INFO

Keywords:
Geostationary SST
Tidal front
Frontal variability
Cloud cover
San Matias Gulf

ABSTRACT

This study investigates the use of Clear Sky Mask (CSKY) and Sea Surface Temperature (SST) products derived from the Advanced Baseline Imager (ABI) sensor onboard the GOES-16 geostationary satellite, focusing on the North Patagonian Gulfs on the Patagonian Shelf, Argentina. The CSKY mask is useful to identify both cloud cover and unreliable SST data, applicable to both the ABI sensor and the VIIRS sensor on the SNPP polar satellite. A three-year analysis of cloud cover revealed extended periods of continuous clear conditions (> 24 h) in the region. During these intervals, SST data from the ABI sensor were validated against those from the VIIRS sensor, showing a spatially coherent structure with a coefficient of determination (R2) of 0.99, albeit with a mean offset of 0.81°C. For the first time, the semidiurnal cycle of the Meridional Front is presented over the mouth of the San Matías Gulf during the warm season. Our findings indicate that this front, referred to as the western front, frequently exhibits semidiurnal displacements that significantly exceed the seasonal and fortnightly variability reported in previous studies. Additionally, towards late summer and into autumn, the presence of an eastern front with similar behavior was observed, resulting in a bi-frontal structure. The separation between these fronts increases towards the end of summer and autumn. Consequently, the ABI GOES-16 offers new opportunities to study the high-frequency variability of fine-scale phenomena in the region.

1. Introduction

In recent years, significant strides have been made in advancing our understanding of surface oceanic processes within the Patagonian Shelf (PS), one of the largest and most productive shelves globally (Fig. 1) (Piola et al., 2018). These advances stem from the integration of diverse data sources, including oceanographic campaign data, Lagrangian observation systems, high-resolution imagery from polar-orbiting satellites, and the use of global reanalyses and regional numerical models (Saraceno et al., 2022). This integration have revealed regional patterns of interannual variability and long-term trends (Allega et al., 2021; Risaro et al., 2022), as well as seasonal (Rivas, 2010) and intra-seasonal (Luz Clara Tejedor et al., 2022) variabilities, submesoscale dynamics (Becker et al., 2023), and synoptic-scale patterns (Pisoni et al., 2014; Valla and Piola, 2015; Carranza et al., 2017) of sea surface temperature (SST). Despite these advances, our understanding of fine-scale structures and their high-frequency variability in this vast geographical region remains limited. The extensive area poses significant challenges for establishing a continuous monitoring system with adequate spatial coverage. Current oceanographic campaigns in the region often lack the temporal continuity necessary to fully capture the evolution of these processes (e.g., Lago et al., 2019 and references therein). While reanalyses and baroclinic models provide valuable information, their spatial and temporal resolutions may not adequately resolve the high-frequency variability of fine-scale structures (e.g., Balmaseda et al., 2013; Madec et al., 2017).

Since the late twentieth century, satellite imagery has been an essential tool for detecting frontal systems on the sea surface. As noted by Acha et al. (2015), fronts are relatively narrow regions that separate water masses with distinct properties and are generated by different forcings. They exhibit high biological productivity, affecting organisms at all trophic levels and providing retention mechanisms for plankton in a highly dispersive environment. Several studies have focused on analyzing frontal systems in the PS (see, for example: Sabatini & Martos,

* Corresponding author at: Servicio Meteorológico Nacional (SMN) de, Argentina.
E-mail address: mdeoto@smn.gob.ar (M. De Oto Proschle).

https://doi.org/10.1016/j.rsma.2024.103920
Received 4 June 2024; Received in revised form 28 October 2024; Accepted 12 November 2024
Available online 15 November 2024

2002; Sabatini et al., 2004; Acha et al., 2004; Saraceno et al., 2004; Rivas, 2006; Romero et al., 2006; Rivas and Pisoni, 2010; Pisoni et al., 2015; Carbajal et al., 2018; Flores-Melo et al., 2018; Piola et al., 2018; Pisoni et al., 2023, among others). Surface thermal fronts, in particular, can be detected by calculating horizontal SST gradients, where relatively high values indicate the presence of regions with sharp temperature variations (Belkin et al., 2009). In the PS, Saraceno et al. (2004) and Rivas and Pisoni (2010) employed this methodology to detect thermal fronts. Notably, tidal fronts are associated with the transition between homogeneous and vertically stratified waters, strongly influenced by turbulent mixing generated by tidal currents and bathymetry (Pisoni et al., 2015). As such, the displacement of the front is expected in response to variations in tidal currents.

In this context, high-resolution images from polar-orbiting satellites have proven useful for the precise identification of thermal fronts across the northern gulfs of the PS, revealing a relationship between their spatial variability and spring and neap tides (Pisoni et al., 2015). However, capturing sub-diurnal variability remains challenging due to the revisit time of polar-orbiting satellites and cloud cover, particularly at high latitudes where cloud frequency is higher, adversely affecting the quality of satellite-derived products (King et al., 2013). Fig. 1 illustrates this scenario, showing the degradation of high-quality SST (shaded) captured in a 'FullDisk' snapshot by the ABI sensor onboard GOES-16 at 18:00 UTC on November 2, 2022.

Unlike sensors on polar-orbiting satellites, geostationary satellites provide continuous coverage with high temporal resolution, allowing for the detection of high-frequency (sub-diurnal) variability (O'carroll et al., 2019). Sensors such as the Advanced Baseline Imager (ABI) on GOES-16 offer good spectral and spatial resolution along with improved temporal resolution, making them invaluable for oceanographic studies. Several studies have demonstrated the suitability of geostationary satellites for assessing sea surface temperature with satisfactory results (e.g., Legeckis et al., 2002; Azevedo et al., 2021; Luo and Minnett, 2021). Furthermore, these satellites have been used to describe small-scale physical processes in near real-time (Hu et al., 2016) and detect persistent upwelling processes (Murphy et al., 2021), among other applications (Seo et al., 2014; Pimentel et al., 2019; Joseph et al., 2021). Despite these advantages, such products have yet to be explored in the PS.

The objective of this work is to assess the validity of the ABI sensor onboard the GOES-16 geostationary satellite for studying temporal variability across different scales of the front located at the mouth of the GSM. The following sections will describe the study area and the data used, detail the ABI sensor in the methodology, and focus on validating the clear-sky mask and SST products. A comparison with the SST data from the VIIRS sensor will follow, along with an analysis of the semi-diurnal and seasonal variabilities of the front located at the mouth of the San Matías Gulf, with the final section reserved for discussion and conclusions.

2. Study area

The study area encompasses the northern region of the Patagonian Shelf, encompassing the southern extent of the El Rincón area (Rincón), San Matías Gulf (SMG), San José Gulf (SJG), Nuevo Gulf (NG), and the shelf area east of the Valdés Peninsula (VP) (see Fig. 1). In this mid-latitude region, winter heat loss at the sea surface promotes water column homogenization and vertical convection, while vertical stratification develops during spring and summer (Rivas, 2010). The SMG, the largest of the North Patagonian gulfs, is a semi-enclosed basin known for its seasonal dynamics. Particularly during the austral summer, it exhibits a cyclonic gyre of approximately 70 km in diameter in the northern part of the gulf (Piola and Scasso, 1988; Tonini et al., 2013).

The tidal regime within the SMG is semidiurnal, with mean amplitudes exceeding 6 m. Notably, the tidal dissipation rate in this area is among the highest in the world (Egbert et al., 2004), significantly contributing to vertical mixing in specific regions throughout the year and leading to the formation of tidal fronts during the summer (Carreto et al., 1986; Rivas and Pisoni, 2010; Pisoni et al., 2015). Palma et al. (2004) and Tonini et al. (2013) report an area of tidal energy dissipation extending eastward from the mouth of the SMG, resulting in the formation of the Valdés tidal front (VF in Fig. 1) and the meridional front on the northern side of the SMG mouth (MF in Fig. 1). According to Pisoni et al. (2015), the MF exhibits a seasonal displacement of approximately 5 km and a fortnightly displacement of up to 10 km during the spring-neap tidal cycle. Additionally, associated with both the VF and

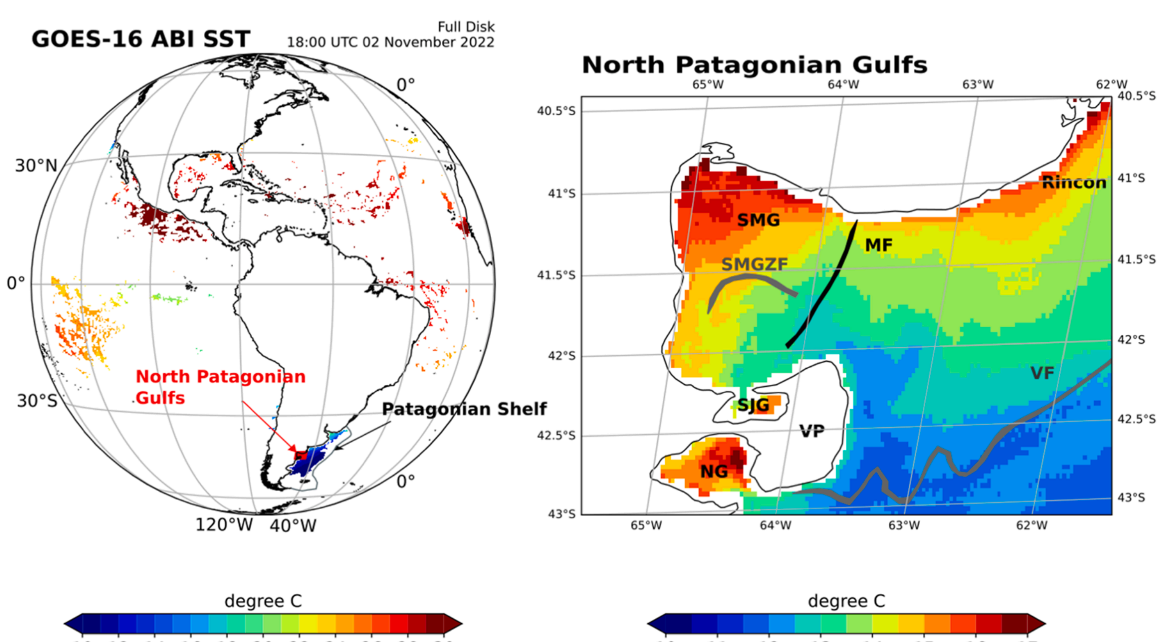

Fig. 1. High-quality of SST product for 18 UTC on November 2, 2022, within the "Full Disk" region of ABI GOES-16 (left panel), highlighting the study area encompassing the North Patagonian gulfs indicated by a red arrow. The right panel overlays the main fronts, including the Valdés Front (VF) depicted by gray line and the Zonal (SMGZF) and Meridional (MF) Fronts of the San Matías Gulf, depicted by gray and black lines, respectively.

MF fronts, a zonal advective front (SMGZF in Fig. 1) develops in the central region of the SMG (Piola and Scasso, 1988; Gagliardini and Rivas, 2004; Pisoni, 2012; Tonini et al., 2013).

3. Data and methodology

The Advanced Baseline Imager (ABI) constitutes a pivotal element onboard the GOES-R program of geostationary satellites (https://www.goes-r.gov/). This state-of-the-art instrument has 16 spectral channels spanning from visible to near-infrared, with the exception of green bands (Schmit et al., 2005; 2017). The spatial resolution of these channels varies from 0.5 to 2 km at nadir, as described in Table 1 of Schmit et al. (2017). In GOES-16's "Full Disk" mode, which covers the study region (Fig. 1), temporal resolution reaches 10 minutes. However, the spatial resolution decreases towards the edges, resulting in an approximate resolution of 3 km in our area of interest (Schmit et al., 2017). At the L2P level, various geophysical products are generated, including clear-sky mask (CSKY) and sea surface skin temperature (hereafter referred to as SST) (Schmit et al., 2017; Kalluri et al., 2018).

The CSKY is derived from 9 of the 16 ABI channels through an algorithm that distinguishes among clear sky, probably clear, cloudy, and probably cloudy conditions, with a temporal resolution of 10 minutes (Heidinger et al., 2020). This product is useful for a wide range of applications, including environmental monitoring and weather forecasting (Schmit et al., 2017). The SST is derived from 5 of the 16 channels using the Advanced Clear Sky Mask Processor for the Ocean (ACSPO) (Petrenko et al., 2010; Kramar et al., 2016). This product is provided with a temporal frequency of 1 h and presents reliable results at the regional level (e.g., Azevedo et al., 2021). In contrast, the Visible Infrared Imaging Radiometer Suite (VIIRS) onboard the Suomi National Polar-orbiting Partnership (SNPP) satellite (Cao et al., 2013) is equipped with 22 spectral channels. SNPP operates with a temporal revisit frequency of approximately 12 hours. The VIIRS SST and its corresponding quality level product are derived through ACSPO preprocessing (Petrenko et al., 2014), making it a widely employed tool in oceanographic research, particularly in regional and local studies.

An overview of the products used in this study is provided in Table 1. The CSKY product categorizes sky conditions into "clear" or "probably clear" (BCM=0) and "cloudy" or "probably cloudy" (BCM=1), while the SST product also provides corresponding quality levels. In contrast, the radiances, which are substantial in data size, were specifically chosen to generate an RGB by-product termed True-Color, as outlined in the methodology described by Miller et al. (2012). ABI sensor data were obtained from the Amazon Web Services (AWS) repository (https://noaa-goes16.s3.amazonaws.com/index.html). SST and their corresponding quality levels from VIIRS were obtained at L2P level and in Near Real-Time (NRT) from NASA OBPG Ocean Color Website (https://oceancolor.gsfc.nasa.gov/cgi/browse.pl?sen=amod).

Table 1
Overview of the satellite product characteristics utilized.

Product	Sensor/ Satellite	Processing Level	Spatial Res.	Temporal Res.
CSKY	ABI/ GOES−16	L2P	~3 km	10 min.
SST	ABI/ GOES−16	L2P	~3 km	1 h
True-Color (1, 2 and 3 Channels)	ABI/ GOES−16	L1B	~3 km	10 min.
SST	VIIRS/SNPP	L2P	750 m	24 h (~18 UTC)

4. Data processing and results

4.1. Validation of the CSKY ABI

A regional qualitative validation of CSKY was conducted to assess its effectiveness as an indicator of cloud cover and as a proxy for SST quality. To achieve this, cloud cover was represented using ABI True-Color imagery, while VIIRS SST quality was used as an indicator of SST degradation. In evaluating VIIRS SST quality, levels classified as "best" and "good" were considered satisfactory, whereas "questionable", "bad" and "not processed" were deemed unsatisfactory. It is important to emphasize that this qualitative validation serves as a cross-validation between ABI and VIIRS sensors, given their concurrent susceptibility to cloud-induced effects. To optimize the validation process, we carefully selected 24 arbitrary dates from 2022, centered around 18 UTC, coinciding with the approximate overpass of the SNPP satellite.

Fig. 2 provides a comprehensive comparison among True-Color imagery (left panel), CSKY (middle panel), and SST quality (right panel) for June 2, 2022, at approximately 18 UTC. The left panel notably captures cloudiness, particularly emphasized east of 64°W longitude. During a cold snap, when dry continental air penetrates the oceanic region, the interaction with the ocean surface destabilizes the continental air mass. This instability promotes convective activity, leading to the formation of open-cell cloud patterns, as observed by Stevens et al. (2005). The imagery reveals consistent spatial correspondence between clear or partially clear skies (center panel) and optimal to good SST quality (right panel), albeit with some discrepancies. Notably, within the eastern sector of the San José and Nuevo Gulfs, suboptimal SST quality persists despite the prevailing clear sky conditions. Conversely, over the MF (Fig. 1), the CSKY image deteriorates, affecting SST quality, even though the True-Color image appears cloud-free. These discrepancies may stem from the ACSPO algorithm, particularly in its handling of high temperature gradients. In this context, Bouali et al. (2020) investigated the influence of cloud masking on frontal regions in the Southwest Atlantic, revealing a significant underestimation of fronts due to inadequate cloud masking. It is also worth noting a temporal discrepancy of 5 minutes in product acquisition (refer to panel titles in Fig. 2) and the approximately 10-minute duration of the ABI sensor scanning.

The comparative visual analysis was extended to the remaining 23 cases (not shown). Only one case, occurring at 17 UTC on December 2, 2022, demonstrated poor VIIRS SST quality due to factors unrelated to cloud cover. Despite this isolated instance, our regional qualitative validation analysis demonstrated a significant relationship between CSKY and both cloud cover and its impact on degrading SST quality, the latter confirmed by cross-referencing with another sensor.

4.2. Validation of SST ABI with SST VIIRS

To compare SSTs using valid data from ABI and VIIRS sensors, the CSKY product was employed at tri-hourly intervals from December 2019 to October 2023. From these datasets, a regional cloud cover fraction (CCF) was derived (Fig. 3 - left panel) by calculating the ratio of the total number of pixels identified as clouds (BCM=1) to the 14,878 pixels corresponding to the oceanic area within the North Patagonian gulfs region (as depicted in Fig. 2). The CCF value reaches 1 when the region is entirely cloudy and 0 when it is completely cloud-free. The distribution of regional cloud cover (Fig. 3 - right panel) exhibits a U-shaped pattern (Rider, 1927), suggesting a binary “off” (cloudless) and “on” (cloudy) behavior. Below the 15th percentile (dashed line in Fig. 3, right panel), the region was considered cloudless. This criterion allowed the identification of 218 events around 18 UTC that were useful for comparing ABI SSTs with VIIRS SSTs.

In Fig. 4, we present a comparison of SST fields between ABI (left panel) and VIIRS (right panel) on March 2, 2022, during one of the cloudless cases. The ABI SST shows a more diffuse pattern with slightly weaker SST gradients compared to VIIRS, mainly due to its lower spatial

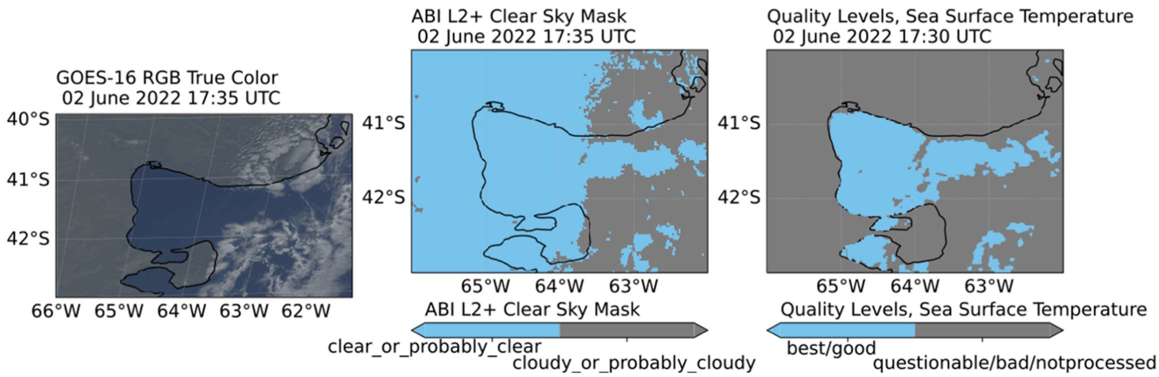

Fig. 2. Images of True-Color (left panel), CSKY (center panel) from ABI, and Quality Levels of SST VIIRS (right panel). Note a 5-minute temporal offset between ABI and VIIRS retrievals.

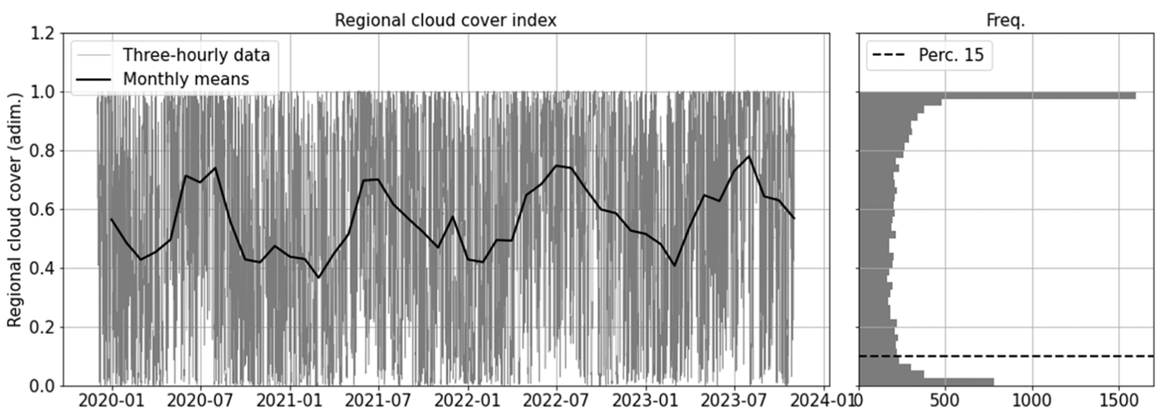

Fig. 3. Regional CCF and Monthly Average (Left Panel) and Histogram depicting the frequency of cloud coverage (Right Panel); The dashed line represents the 15th Percentile, indicating clear conditions.

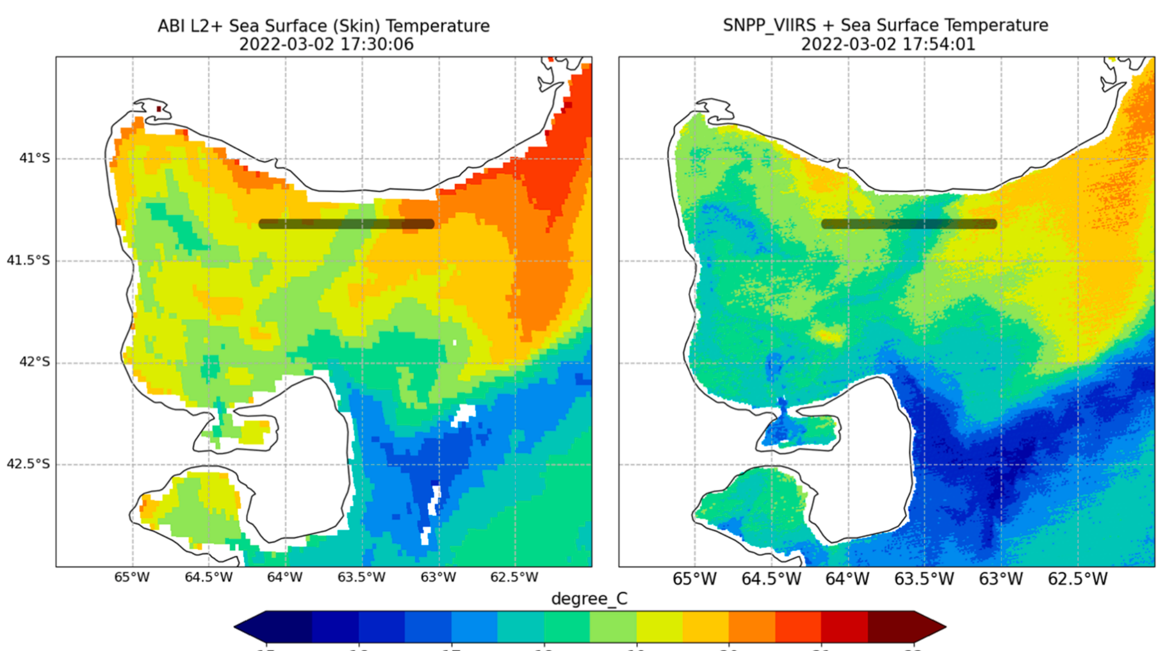

Fig. 4. SST comparison on March 2, 2022, between ABI (left panel) and VIIRS (right panel) during clear sky conditions defined by the 15th percentile of regional CCF (see Fig. 3). Noteworthy are the temporal discrepancies: ABI acquisition approximately 30 minutes before 18 UTC, VIIRS approximately 6 minutes before, resulting in a 24-minute difference between the two sensors (see subtitles). The shaded area represents the zonal polygon spanning the MF.

resolution. Both images reveal well-defined fine features, including the front at the mouth of the SMG (as shown in Fig. 1, and Pisoni et al., 2015) and the cold eddy at 42°S - 64.5°W associated with the outflow of water from the SJG (Amoroso and Gagliardini, 2010). With a pixel-to-pixel spacing of 600 m, we obtained 8063 matches, revealing mean SST values of 18.75°C for ABI and 18.08°C for VIIRS, with a coefficient of determination (R2) of 0.95. This indicates a positive bias in ABI SST compared to VIIRS, as depicted in Fig. 4. Nevertheless, the spatial coherence of SSTs remains consistent across both sensors.

Fig. 5 shows SST statistics derived from a total of 1,352,686 matches from 218 fields under clear-sky conditions, using both ABI and VIIRS datasets. SST dispersion between VIIRS and ABI sensors increases with higher SST values (Fig. 5a), demonstrating a positive bias and a normal distribution centered around 0.81°C (Fig. 5d). The coefficient of determination (R^2) shows high values, exceeding 0.98, with a slight decrease toward the coast (Fig. 5b). As expected, bias increases with the acquisition time difference (Fig. 5c) but remains consistent around the mean bias of 0.81°C (Fig. 5d). Under clear sky conditions and with an extensive dataset, these findings show that ABI SST exhibits a positive bias and a more diffuse pattern compared to VIIRS. However, ABI consistently captures spatial structure and contrasts, which is crucial for discerning the detailed spatial features of the MF. Additionally, ABI's improved temporal resolution represents a significant advancement over previous studies, as it enables the detection of variability on an hourly scale.

4.3. Semidiurnal variability of the MF

The CCF was used to identify extended periods of continuous clear intervals (P15, Fig. 3). Each of these intervals was chosen to exceed 24 hours and encompass two tidal cycles. Between December 2019 and October 2023, a total of 38 cases met these criteria. The modal duration of these intervals is approximately 35 hours, and two of them lasted approximately 75 hours (Fig. 6). These cases are distributed throughout the year, except for May, June, and July (Fig. 6, upper corner). As demonstrated by Rivas et al. (2006), increased cloud cover during these months (see Fig. 3) inhibits visible and infrared satellite observations of the ocean surface.

The initial step in determining the position of the MF involved identifying areas with high SST contrasts through the following algorithm:

1) For each clear sky interval, SST was averaged meridionally within a polygon centered at 41.32°S, spanning a width of 0.05° and extending zonally from 63.05°W to 64.15°W (refer to Fig. 4), similar to the methodology employed by Pisoni et al. (2015).
2) A Hovmöller diagram was constructed, representing the meridionally averaged SST as a function of longitude and time.
3) The logarithm of the absolute SST gradient was calculated across the Hovmöller diagram. Regions where the gradient exceeded the 90th percentile were identified as significant SST contrasts, potentially indicating SST front candidates.

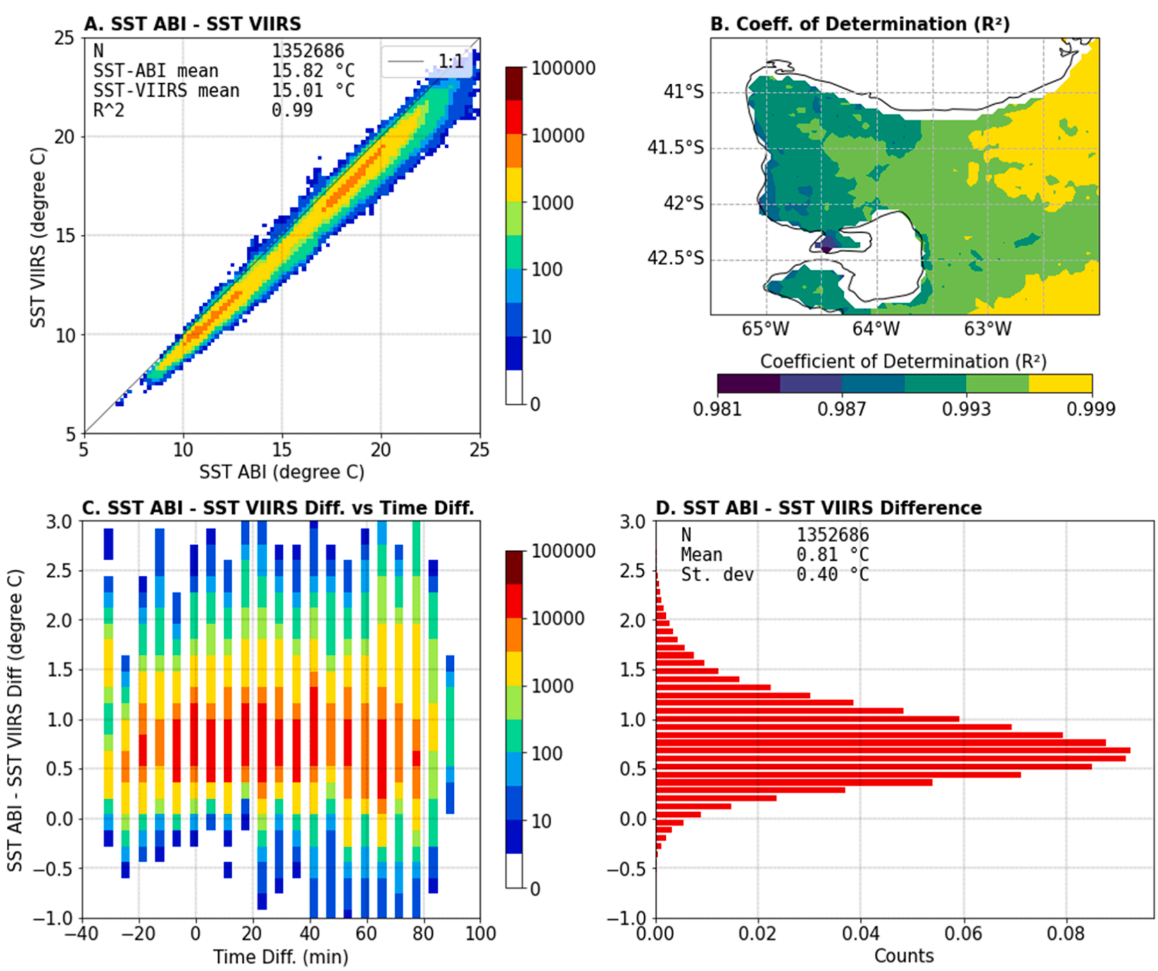

Fig. 5. SST matches between ABI and VIIRS: (A) Linear regression between SST, (B) Coefficient of Determination, (C) SST differences as a function of the temporal acquisition differences, and (D) Distribution of difference (see subtitles).

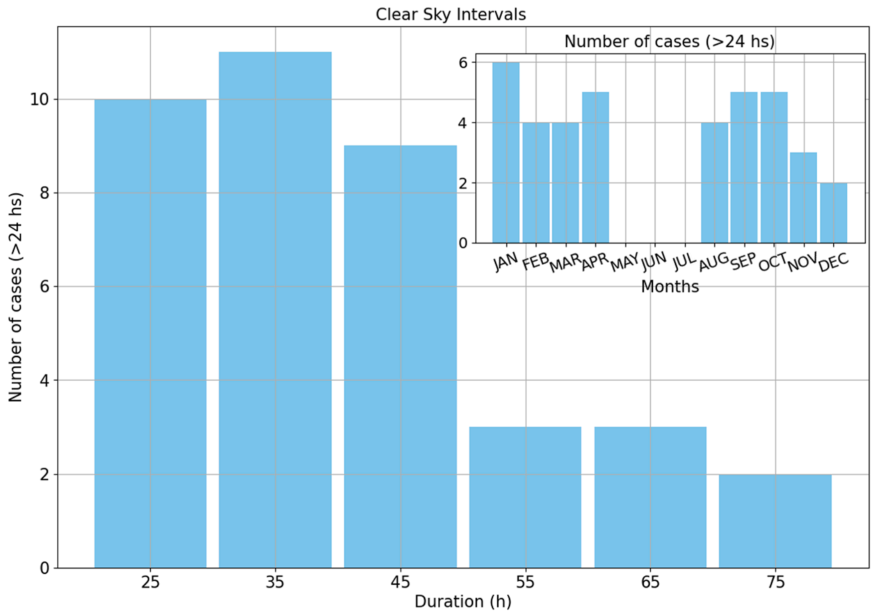

Fig. 6. Distribution of the duration (in hours) of 38 cases of continuous clear intervals (<P15), each lasting more than two tidal cycles (>24 hours), along with their seasonal occurrence displayed in the right panel.

The 90th percentile threshold in the logarithm of the absolute SST gradient is advantageous in filtering out weak and spurious thermal gradients that might be incorrectly associated with frontal regions. However, the effectiveness of this threshold is influenced by both seasonal variability and the unique characteristics of the study area, complicating the definitive identification of a tidal front. To address this, two filtering mechanisms were introduced: (i) *temporal persistence* and (ii) *intensity criterion*. The *temporal persistence* filter was designed to capture the dynamic nature of tidal fronts by requiring a sustained SST gradient over most of continuous clear intervals. The filter resulted in the exclusion of 4 out of the 38 cases. On the other hand, the intensity criterion was set at a minimum gradient of 0.05 °C/km, based on both the literature (Rivas and Pisoni, 2010) and from the analysis with the current SST dataset. This analysis consisted of determining the 90th percentile of the SST gradient from a mean histogram of the 38 cases, resulting in a value of 0.049 °C/km, which we rounded to 0.05 °C/km. This criterion effectively acts as a seasonal filter, particularly identifying gradients that prevail during winter, when the water column generally exhibits vertical homogeneity. As a result, 9 cases were eliminated based on this criterion, predominantly observed during the cold season (August). After applying both filters, a total of 25 frontal cases were retained from the 38 continuous clear intervals, constituting 66 % of the dataset.

Fig. 7 illustrates the semidiurnal variability of the meridional front observed in one of the 25 cases, specifically from 22nd to 24th February 2020. The figure includes the Hovmöller diagram of SST (Fig. 7a), tidal height (Fig. 7b), meteorological variables such as wind speed and air temperature (Fig. 7c), and bathymetry (Fig. 7d). The tidal series was computed using the eight primary regional tidal components from the TPXO model (Egbert and Erofeeva, 2002). Wind speed at 10 m and air temperature at 2 m (Ta) were extracted from the ERA5 reanalysis (Hersbach et al., 2020), while bathymetry data was obtained from the GEBCO 2021 model (GEBCO Bathymetric Compilation Group (2021)), enabling a dynamic analysis of the tidal front. Both tidal and meteorological variables were computed or extracted from a hypothetical position representing the mean position of the front (41.32 °S and 63.60 °W). The Hovmöller plot was generated by averaging the SST following the previously described algorithm, which allowed for the positioning of the front's location (Log(grad(SST))) > 90th percentile) from the computation of a histogram (Fig. 7e) of its location.

In the case corresponding to the period from February 22–24, 2020 (Fig. 7), the presence of the MF is evident as a bi-frontal structure, consisting of a western front located at 63.79°W and an eastern front at 63.47°W (dashed lines), with a separation of approximately 26.7 km. This bi-frontal structure exhibits periodic oscillations in phase with the tidal cycle (Fig. 7b), showing a more pronounced westerly displacement during high tide, which coincides with the inflow of shelf water into the gulf. This phenomenon suggests that tidal currents advect the front, causing it to reach its westernmost position following the complete influx of water into the gulf. The histogram (Fig. 7e) depicts the most frequent positions (in hours) of both fronts. While the western front is widely recognized in the literature as a tidal front influenced by bathymetric gradients (Fig. 7d), the eastern front is situated in a region of nearly constant depth. During this period, the identification of the bi-frontal structure becomes less distinct during the daily thermal cycle, particularly at SST peaks around 18 UTC (15 local time), which occur before the maximum Ta (red line in Fig. 7c), and during periods of weak winds (< 5 m/s, green line in Fig. 7c). Notably, the SST maximum initially appears in the eastern sector and then extends to the western sector with a lag of up to 3 hours. Additionally, it is noteworthy that the definition of the front becomes increasingly distinct over time, likely corresponding to the rise in Ta.

To obtain a more detailed description of the bi-frontal structure during the event from February 22–24, 2020, the SST field (Fig. 8 and animation loop in the supplemental material) was plotted over one tidal cycle. The 18.5°C and 19°C isotherms (contours) were used as instantaneous tracers of frontal positions, while mean positions (depicted by red lines) derived from the histograms in Fig. 7e were also included. Fig. 8 illustrates the westward displacement of the bi-frontal structure until 3 UTC on February 23, followed by an eastward oscillation until 9 UTC the same day. During this sequence, the zonal displacement reached 19.2 and 17.5 km for the western and eastern fronts, respectively.

The 24 remaining cases similar to Fig. 7 are presented in supplemental material (see Figs. S1 to S24).

4.4. Seasonal variability of the MF

Table 2 quantifies the seasonal occurrence of the MF based on the detection of 25 frontal structures, applying intensity and persistence

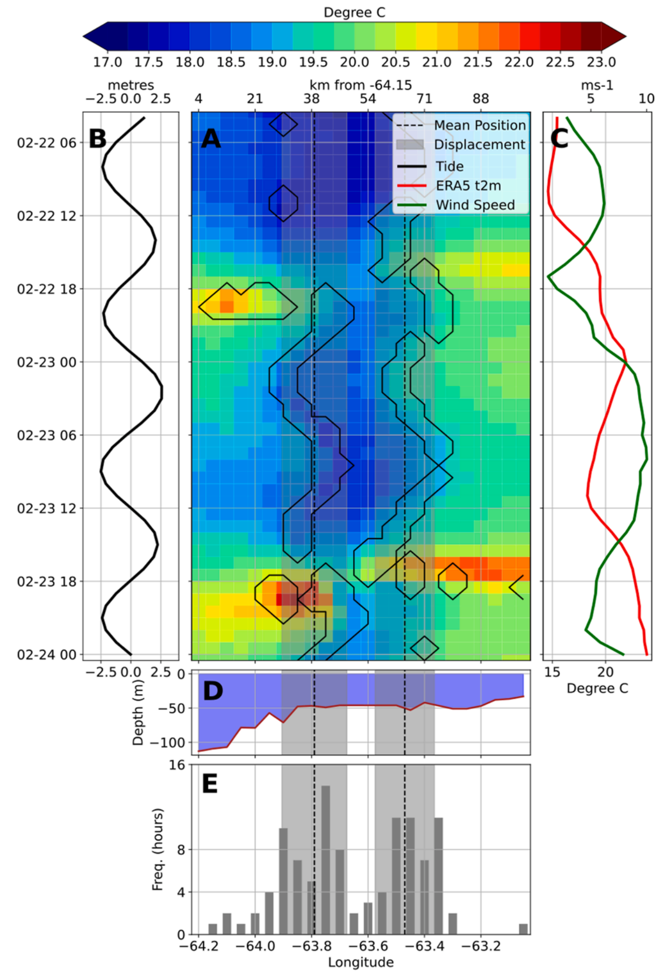

Fig. 7. (a) Hovmöller diagram showing ABI SST (shaded) and frontal position (contour); (b) Astronomical tide at 41.32°S and 63.60°W; (c) Time series of 10 m wind speed (green) and ERA 5 air temperature (red); (d) GEBCO bathymetry within the polygon where the Hovmöller diagram was computed (as shown in Fig. 4); and (e) Histogram displaying the frequency (in hours) of front location during the clear interval from February 22–24, 2020. The upper axis, measured in kilometers, represents the distance from longitude 64.15°W.

filters to both the western front and the bi-frontal structure. Notably, no cases were detected during winter, when vertical mixing of the water column inhibits the formation of the tidal front. The predominant frontal structure observed is the western front, identified in 19 cases. In the remaining cases, a second frontal structure, the eastern front, is observed simultaneously, forming what is referred to as a bi-frontal structure. This bi-frontal configuration is most common from late summer to autumn.

A correlation analysis between tidal height and front displacement revealed a significant direct relationship, indicating that higher tidal heights, particularly during spring tides, result in greater front displacement (see Fig. S25 in the supplemental material), consistent with findings by Pisoni et al., (2015). Conversely, no significant correlations were found between atmospheric variables and front displacement, suggesting that these variables have less influence on the front's location, although they may play a role in its erosion. Additionally, the plots show seasonal variation in the mean position of the front, reaching its easternmost extent during summer (red dots in the central panels), regardless of the atmospheric conditions considered.

Fig. 9 shows the time series of the positions of the western front (red) and the eastern front (blue) over the analysis period. The figure reveals a clear eastward shift of the western front, reaching its easternmost position during summer, followed by a slight westward retraction, consistent with the findings reported by Pisoni et al. (2015). In contrast, the eastern front, detected sporadically, generally appears more frequently towards the end of summer and autumn, contributing to the formation of the bi-frontal structure. No frontal occurrences were found during the winter months.

Fig. 10 shows the images corresponding to each of the six identified occurrences of the bi-frontal structure, as described in Table 2 and represented in Fig. 9. Different isotherms (contours) and markers indicating the mean position (highlighted in red) are used to highlight the frontal locations.This method clearly distinguishes the positions of both fronts, showing an increase in their separation from summer to autumn, and highlighting their proximity in the single spring occurrence. During the transition from summer to autumn, the separation distance between the two fronts gradually increases, ranging from 15 to 60 km, with an average of 38.5 km.

4.5. *Frontogenesis and frontolysis events of the MF*

During spring, as the front develops, its persistence weakens, making it susceptible to changes in atmospheric forcing, which can impact its structure. This section analyzes the relationship between front detection, tidal height, and atmospheric variables during spring 2022, when frontogenesis and frontolysis events associated with synoptic-scale events were observed.

Fig. 11 shows the synoptic variability of the front using Hovmöller diagrams for five cases of continuous clear intervals occurring between September and November 2022. To accurately reference the solar cycle, the time axis is expressed in UTC hours from 00Z on the first day of each interval. In early austral spring (cases a and b in Fig. 11, respectively), intermittent frontal structures with relatively high SST gradients (contours) are observed. Towards the end of September (case c in Fig. 11), a well-developed tidal front was observed for over two days, with a temperature gradient reaching up to 0.12°C/km and a displacement of 19.2 km near 63.95°W. The front disappears in mid-October (case d in Fig. 11), when a more intense front might be expected due to the seasonal increase in heat flux and vertical stratification. Finally, at the beginning of November (case e in Fig. 11), the front fully develops, although its intensity remains lower than that observed at the end of September (case c). Notably, there is an eastward displacement of the front by 18.3 km, positioning it around 63.92°W. This is consistent with the seasonal displacement mentioned by Pisoni et al. (2015). Unlike the event at the end of summer 2020 (see Fig. 7), no bi-frontal structure was observed during spring 2022.

To describe the sensitivity of the front during the spring of 2022, tidal height, Ta, wind speed and direction were considered (Fig. 12). In all cases in Fig. 11, the tidal height was approximately 6 m, except in case e, where it was about 1 m lower. The SST (blue in Fig. 12b) was observed to be slightly higher than Ta (red in Fig. 12b) in cases a, b, and d, contrary to cases c and e). In case c, wind intensified towards the end of the observation period, during which a more diffuse front was observed. A similar phenomenon was observed towards the end of spring (case e) with a higher northeasterly wind speed (barbs), suggesting that stronger winds make surface front detection more challenging. Additionally, in the latter case, a lower tidal height was recorded compared to case c, which may be linked, as suggested by Fig. 11, to reduced frontal displacement. It is noteworthy that the maximum wind intensity ($>$ 15 m/s) occurred prior to case D, during which the frontal system appears significantly weakened.

In summary, wind speed and the difference between SST and Ta appear to be factors affecting the satellite observation of the front, at least during this study period. These variables, related to the sensible heat flux, may have been crucial in the frontal disappearance observed in case d, where the most intense wind period of the series was previously recorded, exceeding 15 m/s with SST-Ta $>$ 0°C, indicating sensible heat loss.

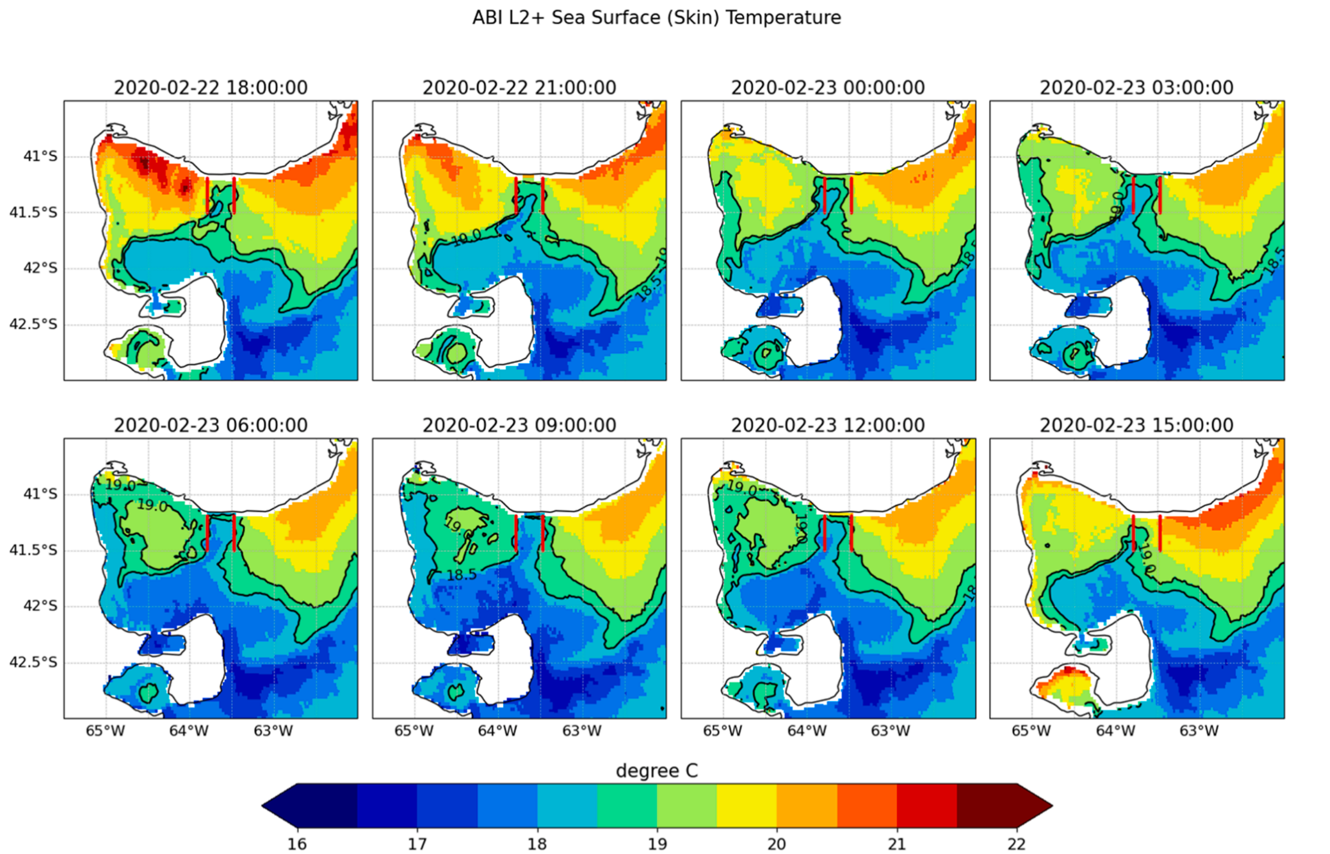

Fig. 8. ABI SST field for the North Patagonian gulfs during the event from February 22–24, 2020 (as shown in Fig. 7). The front position is delineated using the 18.5°C and 19°C isotherms (contours), with the mean positions of the western and eastern fronts (as depicted in Fig. 7a) represented by two meridional lines (in red).

Table 2
Frontal characteristics of the MF as a function of seasonality. Note that no frontal occurrences were found during the winter months.

	Total Cases	West Front Only	Bi-front
Spring	7	6	1
Summer	12	10	2
Autumn	6	3	3
All	25	19	6

5. Discussion and conclusions

This study investigated the high-frequency variability of the Meridional Front (MF) in the San Matias Gulf using high-resolution Clear Sky Mask (CSKY) and sea surface temperature (SST) products from the ABI sensor onboard the GOES-16 satellite. The CSKY product was utilized to optimize SST case selection for validation against a traditional polar-orbiting sensor (VIIRS), revealing a strong regional correlation between the two sensors. Despite a positive bias of approximately 0.8°C, both products accurately represented the spatial structure of the SST field, underscoring the ABI SST product's reliability for regional studies at mid-latitudes. By combining cloud cover and SST quality assessments, CSKY enabled the identification of 25 study cases, providing a detailed high-frequency description of regional SST behavior over the MF.

The MF becomes detectable in early spring at the mouth of the gulf due to increased heat flux into the ocean, which causes vertical stratification of the gulf waters, which are deeper than those at the mouth and adjacent shelf. During this time, the front is still sensitive to heat exchanges with the atmosphere, which may limit its surface detection. As spring progresses into summer, the front intensifies and moves slightly

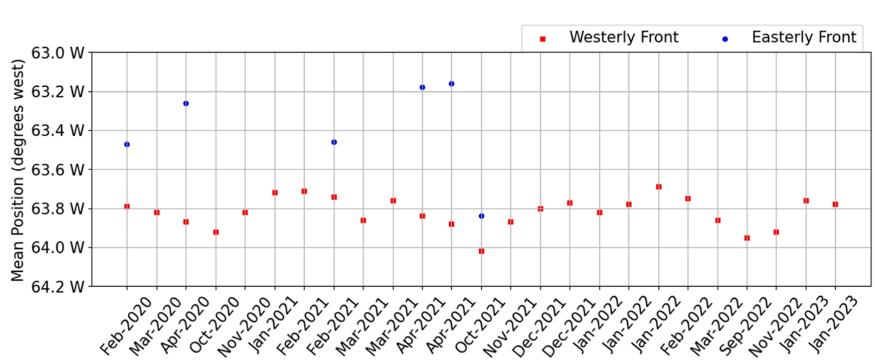

Fig. 9. Temporal evolution of the western front (in red) and eastern front (in blue) positions throughout the study period. Note that the time scale is not uniform and no frontal occurrences are detected in winter months.

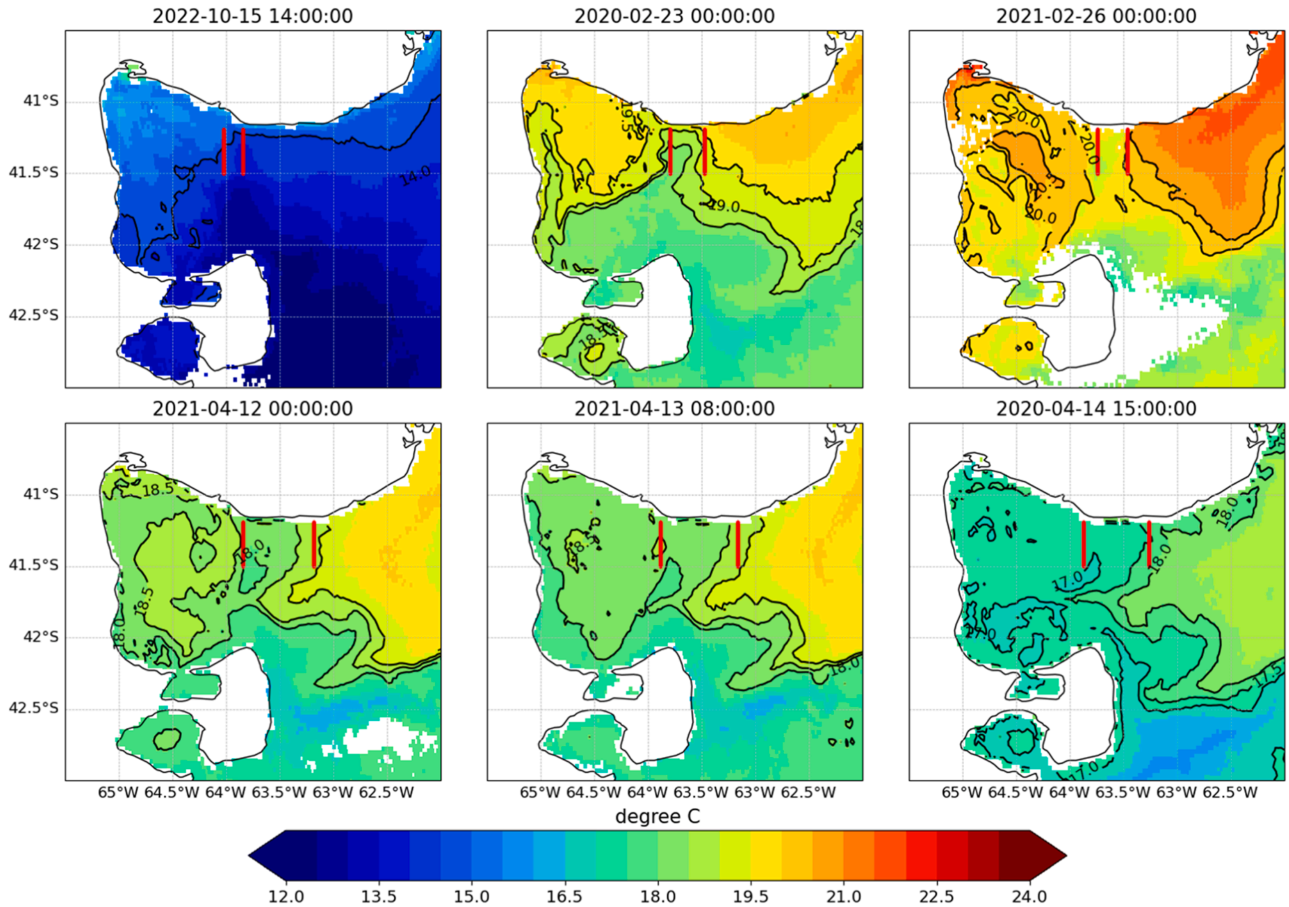

Fig. 10. Hourly snapshots of SST (shaded) for the six cases (as indicated in the title) where the bi-frontal structure was detected. The red meridional lines denote the average positions of the western and eastern fronts during periods of continuous clear intervals.

eastward.

Although frontal development is a typical case of tidal fronts, where tidal energy dissipation homogenizes the water column to a certain depth (approximately 70 m in this region according to Pisoni et al., 2015), by late summer, a bi-frontal structure develops with an eastern front located outside the gulf mouth in a shallower region (~50 m). These relatively high gradients suggest the presence of a thermal front that should not, in principle, be associated with a typical tidal front, as both sides of the front should exhibit vertically homogeneous water columns (see Fig. S26 in the supplemental material). Nevertheless, its displacement is equally influenced by tidal height, as observed in Fig. 7. A similar behavior was detected in late summer north of the Valdés front, where relatively high SST gradients were observed in a region where the water column remains vertically homogeneous throughout the year (Pisoni, 2012). These high gradients were associated with the southwestward advection of warmer coastal waters, inferred from in-situ data analysis (Lucas et al., 2005). In autumn, the bi-frontal structure becomes the most prominent feature of the frontal system.

For the first time, the semidiurnal spatial displacement of the MF was quantified. The western front's average semidiurnal displacement is around 20.8 km, which exceeds the seasonal and fortnightly variability reported by Pisoni et al. (2015). Given that this displacement is due to the 6-hour tidal flood or ebb flow, the average current magnitude in the northern sector of the MF is estimated to be approximately 1 m/s. This value is about half of the maximum M2 tidal current component reported by numerical simulations (Tonini and Palma, 2017), which is reasonable. In comparison, Hopkins and Polton (2012) observed 5–10 km variations in the Liverpool Bay front driven by tidal currents. Chevallier et al. (2014) reported a semidiurnal spatial variability of approximately 7.3 km for the Ushant tidal front. Carbajal et al. (2018) documented semidiurnal variations of about 3.9 km in intermediate tides and 8.9 km close to spring tides for the San Jorge Gulf, with bottom front displacements being 30–40 % greater than those at the surface.

This study also included an analysis of the possible influence of atmospheric conditions on the weakening of the front during spring when it is forming. This could lead to intermittent frontal detection, as suggested by Czitrom and Simpson (1998). For future work, it is recommended to use a regional circulation model to analyze the impact of different forcings on frontal displacement.

Finally, the high temporal frequency of GOES-16 imagery provides a valuable tool for studying high-frequency dynamics on the Patagonian shelf. This capability is particularly important for understanding the spatial dynamics of frontal systems across semidiurnal and seasonal scales. Furthermore, it can play a significant role in aiding decision-makers in the establishment and expansion of marine protected areas, as evidenced by recent initiatives involving the Valdés front (see for example: https://rb.gy/1oiykv).

Code

The retrieval of CSKY data from AWS servers and its subsequent processing, along with examples of usage in the study region, can be accessed at https://gitlab.com/mdeotoproschle/goes_sst.

CRediT authorship contribution statement

Matias De Oto Proschle: Writing – review & editing, Writing – original draft, Visualization, Supervision, Methodology, Investigation,

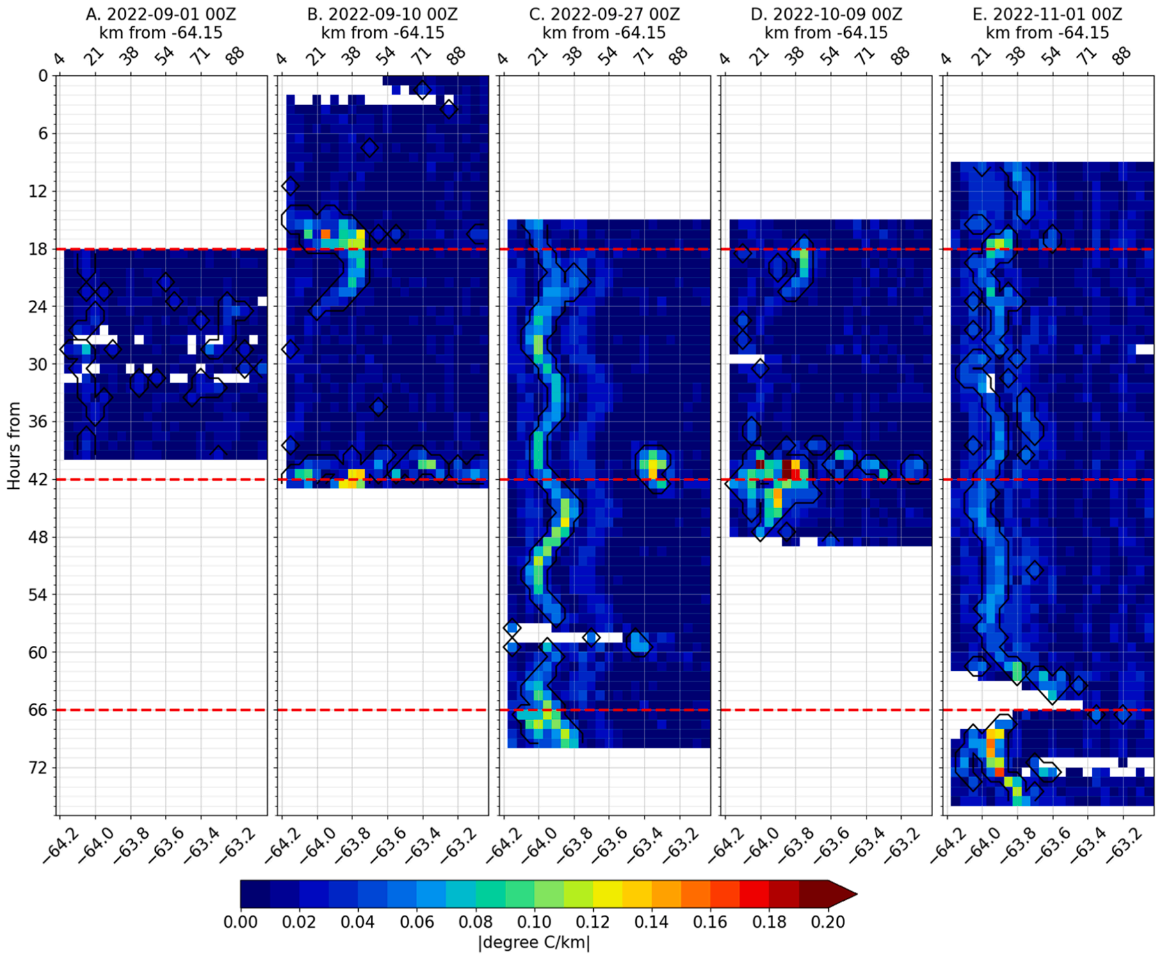

Fig. 11. Hovmöller of the absolute SST gradient (shaded) and frontal location (contours) around the transect of the MF (see Fig. 1) for early (a), mid (b), and late (c) September, mid-October (d), and early November (e) of the austral spring 2022. White pixels represent data that is masked due to reasons other than cloudiness. For better visualization, the temporal and SST scales have been preserved. The time axis shows hours from 00Z of the day of the clear interval (see titles) and the dashed lines represent 15 UTC local time for each day.

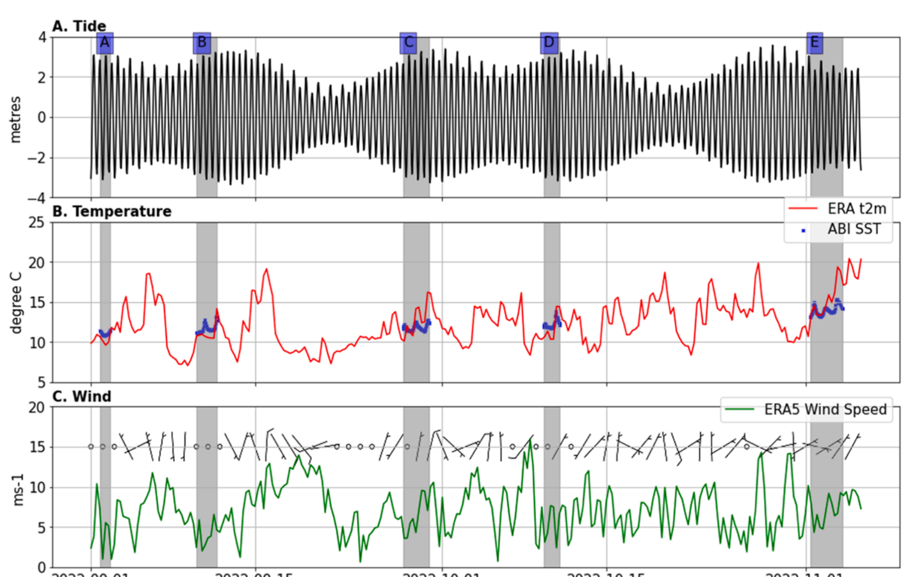

Fig. 12. Variability of astronomical tide (panel a), Ta and SST (panel b), and wind intensity (m/s) and direction (wind barbs) (panel c) at 41.32°S and 63.60°W during the highlighted periods in Fig. 11 (shaded).

Formal analysis, Data curation, Conceptualization. **Sofia Muñoz:** Writing – review & editing, Writing – original draft, Visualization, Methodology, Data curation, Conceptualization. **Violeta Valdeomillos:** Writing – review & editing, Writing – original draft, Visualization, Methodology, Data curation, Conceptualization. **Juan Pablo Pisoni:** Writing – review & editing, Writing – original draft, Visualization, Supervision, Project administration, Methodology, Investigation, Formal analysis, Data curation, Conceptualization.

Declaration of Competing Interest

The authors declare that they have no conflict of interest

Acknowledgments

We extend our gratitude to Professor Silvia Romero for her motivation and exceptional support throughout the completion of this work, particularly during the course "Satellite Remote Sensing and Oceanographic Applications" offered by DCAO-FCEyN/UBA. We would like to thank Dr. Luciano Vidal from SMN for providing the initial insight into the ABI/GOES sensor. We also thank the anonymous reviewers, whose comments have substantially improved the quality of this article. Finally, we extend our thanks to the PronoMAr project (PIDT A5) and the Fund for Scientific and Technological Research (PICT-2021-GRF-TI-00459).

Appendix A. Supporting information

Supplementary data associated with this article can be found in the online version at doi:10.1016/j.rsma.2024.103920.

Data availability

Data will be made available on request.

References

Acha, E.M., Mianzan, H.W., Guerrero, R.A., Favero, M., Bava, J., 2004. Marine fronts at the continental shelves of austral South America: physical and ecological processes. J. Mar. Syst. 44 (1-2), 83–105.
Acha, E.M., Piola, A., Iribarne, O., Mianzan, H., 2015. Ecological processes at marine fronts: oases in the ocean. Springer.
Allega, L., Pisoni, J.P., Cozzolino, E., Maenza, R.A., Piccolo, M.C., 2021. The variability of sea surface temperature in the patagonian shelf Argentina, from 35 years of satellite information. Int. J. Remote Sens. 42 (16), 6090–6106.
Amoroso, R.O., Gagliardini, D.A., 2010. Inferring complex hydrographic processes using remote-sensed images: turbulent fluxes in the patagonian gulfs and implications for scallop metapopulation dynamics. J. Coast. Res. 26 (2), 320–332.
Azevedo, M.H., Rudorff, N., Aravéquia, J.A., 2021. Evaluation of the ABI/GOES-16 SST product in the tropical and Southwestern Atlantic Ocean. Remote Sens. 13 (2), 192.
Balmaseda, M.A., Mogensen, K., Weaver, A.T., 2013. Evaluation of the ECMWF ocean reanalysis system ORAS4. Q. J. R. Meteorol. Soc. 139 (674), 1132–1161.
Becker, F., Romero, S.I., Pisoni, J.P., 2023. Detection and characterization of submesoscale eddies from optical images: a case study in the Argentine continental shelf. Int. J. Remote Sens. 44 (10), 3146–3159.
Belkin, I.M., Cornillon, P.C., Sherman, K., 2009. Fronts in large marine ecosystems. Prog. Oceanogr. 81 (1-4), 223–236.
Bouali, M., Polito, P.S., Sato, O.T., Bernardo, P.S., Vazquez-Cuervo, J., 2020. The impact of cloud masking on the climatology of sea surface temperature gradients. Remote Sens. Lett. 11 (12), 1110–1117.
Cao, C., De Luccia, F.J., Xiong, X., Wolfe, R., Weng, F., 2013. Early on-orbit performance of the visible infrared imaging radiometer suite onboard the Suomi National Polar-Orbiting Partnership (S-NPP) satellite. IEEE Trans. Geosci. Remote Sens. 52 (2), 1142–1156.
Carbajal, J.C., Rivas, A.L., Chavanne, C., 2018. High-frequency frontal displacements south of San Jorge Gulf during a tidal cycle near spring and neap phases: biological implications between tidal states. Oceanography 31 (4), 60–69.
Carranza, M.M., Gille, S.T., Piola, A.R., Charo, M., Romero, S.I., 2017. Wind modulation of upwelling at the shelf-break front off Patagonia: observational evidence. J. Geophys. Res.: Oceans 122 (3), 2401–2421.
Carreto, J.I., Benavides, H.R., Negri, R.M., Glorioso, P.D., 1986. Toxic red-tide in the Argentine Sea. Phytoplankton distribution and survival of the toxic dinoflagellate Gonyaulax excavata in a frontal area. J. Plankton Res. 8 (1), 15–28.
Chevallier, C., Herbette, S., Marié, L., Le Borgne, P., Marsouin, A., Péré, S., Reason, C., 2014. Observations of the Ushant front displacements with MSG/SEVIRI derived sea surface temperature data. Remote Sens. Environ. 146, 3–10.
Czitrom, S.P.R., Simpson, J.H., 1998. Intermittent stability and frontogenesis in an area influenced by land runoff. J. Geophys. Res.: Oceans 103 (C5), 10369–10376.
Egbert, G.D., Erofeeva, S.Y., 2002. Efficient inverse modeling of barotropic ocean tides. J. Atmos. Ocean. Technol. 19 (2), 183–204.
Egbert, G.D., Ray, R.D., Bills, B.G., 2004. Numerical modeling of the global semidiurnal tide in the present day and in the last glacial maximum. J. Geophys. Res.: Oceans 109 (C3). https://doi.org/10.1029/2003JC001973.
Flores-Melo, X., Schloss, I.R., Chavanne, C., Almandoz, G.O., Latorre, M., Ferreyra, G.A., 2018. Phytoplankton ecology during a spring-neap tidal cycle in the southern tidal front of San Jorge Gulf. Patagon. Oceanogr. 31 (4), 70–80.
Gagliardini, D.A., Rivas, A.L., 2004. Environmental characteristics of San Matías Gulf obtained from LANDSAT-TM and ETM+ data. Gayana (ConcepciónN.) 68 (2), 186–193.
GEBCO Bathymetric Compilation Group (2021). A continuous terrain model of the global oceans and land, NERC EDS British Oceanographic Data Centre NOC. doi:10.5285/c6612cbe-50b3-0cff-e053-6c86abc09f8f, 2021.
Heidinger, A.K., Pavolonis, M.J., Calvert, C., Hoffman, J., Nebuda, S., Straka III, W., Wanzong, S., 2020. ABI cloud products from the GOES-R series. In The GOES-R Series. Elsevier, pp. 43–62.
Hersbach, H., Bell, B., Berrisford, P., Hirahara, S., Horányi, A., Muñoz-Sabater, J., Thépaut, J.N., 2020. The ERA5 global reanalysis. Q. J. R. Meteorol. Soc. 146 (730), 1999–2049.
Hopkins, J., Polton, J.A., 2012. Scales and structure of frontal adjustment and freshwater export in a region of freshwater influence. Ocean Dyn. 62, 45–62.
Hu, Z., Pan, D., He, X., Bai, Y., 2016. Diurnal variability of turbidity fronts observed by geostationary satellite ocean color remote sensing. Remote Sens. 8 (2), 147.
Joseph, J., Girishkumar, M.S., Varikoden, H., Thangaprakash, V.P., Shivaprasad, S., Rama Rao, E.P., 2021. Observed sub-daily variability of latent and sensible heat fluxes in the Bay of Bengal during the summer. Clim. Dyn. 56, 917–934.
Kalluri, S., Alcala, C., Carr, J., Griffith, P., Lebair, W., Lindsey, D., Zierk, S., 2018. From photons to pixels: processing data from the advanced baseline imager. Remote Sens. 10 (2), 177.
King, M.D., Platnick, S., Menzel, W.P., Ackerman, S.A., Hubanks, P.A., 2013. Spatial and temporal distribution of clouds observed by MODIS onboard the Terra and Aqua satellites. IEEE Trans. Geosci. Remote Sens. 51 (7), 3826–3852.
Kramar, M., Ignatov, A., Petrenko, B., Kihai, Y., Dash, P., 2016. Near real time SST retrievals from Himawari-8 at NOAA using ACSPO system (May). In: In Ocean Sensing and Monitoring VIII, 9827. SPIE, pp. 149–159 (May).
Lago, L.S., Saraceno, M., Martos, P., Guerrero, R.A., Piola, A.R., Paniagua, G.F., Provost, C., 2019. On the wind contribution to the variability of ocean currents over wide continental shelves: a case study on the northern Argentine continental shelf. J. Geophys. Res.: Oceans 124 (11), 7457–7472.
Legeckis, R., Brown, C.W., Chang, P.S., 2002. Geostationary satellites reveal motions of ocean surface fronts. J. Mar. Syst. 37 (1-3), 3–15.
Lucas, A.J., Guerrero, R.A., Mianzan, H.W., Acha, E.M., Lasta, C.A., 2005. Coastal oceanographic regimes of the northern Argentine continental shelf (34–43 S). Estuar., Coast. Shelf Sci. 65 (3), 405–420.
Luo, B., Minnett, P.J., 2021. Skin sea surface temperatures from the GOES-16 ABI validated with those of the shipborne M-AERI. IEEE Trans. Geosci. Remote Sens. 59 (12), 9902–9913.
Luz Clara Tejedor, M., Alvarez, M.S., Vera, C., Simionato, C.G., Jaureguizar, A.J., 2022. Relationship between sea surface temperature anomalies in the Southwestern Atlantic Continental Shelf and atmospheric variability on intraseasonal timescales. Clim. Dyn. 59 (5), 1539–1554.
Madec, G., Bourdallé-Badie, R., Bouttier, P.A., Bricaud, C., Bruciaferri, D., Calvert, D., … & Vancoppenolle, M.. (2017). NEMO ocean engine. https://doi.org/10.5281/zenodo.3248739.
Miller, S.D., Schmidt, C.C., Schmit, T.J., Hillger, D.W., 2012. A case for natural colour imagery from geostationary satellites, and an approximation for the GOES-R ABI. Int. J. Remote Sens. 33 (13), 3999–4028.
Murphy, S.C., Nazzaro, L.J., Simkins, J., Oliver, M.J., Kohut, J., Crowley, M., Miles, T.N., 2021. Persistent upwelling in the Mid-Atlantic Bight detected using gap-filled, high-resolution satellite SST. Remote Sens. Environ. 262, 112487.
O'carroll, A.G., Armstrong, E.M., Beggs, H.M., Bouali, M., Casey, K.S., Corlett, G.K., Wimmer, W., 2019. Observational needs of sea surface temperature. Front. Mar. Sci. 6, 420.
Palma, E.D., Matano, R.P., Piola, A.R., 2004. A numerical study of the Southwestern Atlantic Shelf circulation: barotropic response to tidal and wind forcing. J. Geophys. Res.: Oceans 109 (C8).
Petrenko, B., Ignatov, A., Kihai, Y., Heidinger, A., 2010. Clear-sky mask for the advanced clear-sky processor for oceans. J. Atmos. Ocean. Technol. 27 (10), 1609–1623.
Petrenko, B., Ignatov, A., Kihai, Y., Stroup, J., Dash, P., 2014. Evaluation and selection of SST regression algorithms for JPSS VIIRS. J. Geophys. Res.: Atmospheres 119 (8), 4580–4599.
Pimentel, S., Tse, W.H., Xu, H., Denaxa, D., Jansen, E., Korres, G., Storto, A., 2019. Modeling the near-surface diurnal cycle of sea surface temperature in the Mediterranean Sea. J. Geophys. Res.: Oceans 124 (1), 171–183.
Piola, A.R., Palma, E.D., Bianchi, A.A., Castro, B.M., Dottori, M., Guerrero, R.A., Saraceno, M., 2018. Physical oceanography of the SW Atlantic Shelf: a review. Plankton Ecol. Southwest. Atl.: Subtrop. subantarctic realm 37–56.
Piola, A.R., Scasso, L.M., 1988. Circulación en el golfo San Matías. Geoacta 15 (1), 33–51.

Pisoni, J.P. (2012). Los sistemas frontales y la circulación en las inmediaciones de los Golfos Norpatagónicos (Doctoral dissertation, Universidad de Buenos Aires. Facultad de Ciencias Exactas y Naturales).
Pisoni, J.P., Rivas, A.L., Piola, A.R., 2014. Satellite remote sensing reveals coastal upwelling events in the San Matías Gulf—Northern Patagonia. Remote Sens. Environ. 152, 270–278.
Pisoni, J.P., Rivas, A.L., Piola, A.R., 2015. On the variability of tidal fronts on a macrotidal continental shelf, Northern Patagonia, Argentina. Deep Sea Res. Part II: Top. Stud. Oceanogr. 119, 61–68.
Pisoni, J.P., Tonini, M.H., Glembocki, N.G., Romero, S.I., Martos, P., 2023. Detection of nearshore topographic eddies and wakes over a macrotidal coastal region. The influence of tidal currents on its generation. Remote Sens. Lett. 14 (6), 585–597.
Rider, P.R., 1927. Analysis of a u-shaped frequency distribution. J. Am. Stat. Assoc. 22 (158), 202–208.
Risaro, D.B., Chidichimo, M.P., Piola, A.R., 2022. Interannual variability and trends of sea surface temperature around southern South America. Front. Mar. Sci. 9, 829144.
Rivas, A.L., 2006. Quantitative estimation of the influence of surface thermal fronts over chlorophyll concentration at the Patagonian shelf. J. Mar. Syst. 63 (3-4), 183–190.
Rivas, A.L., 2010. Spatial and temporal variability of satellite-derived sea surface temperature in the southwestern Atlantic Ocean. Cont. Shelf Res. 30 (7), 752–760.
Rivas, A.L., Dogliotti, A.I., Gagliardini, D.A., 2006. Seasonal variability in satellite-measured surface chlorophyll in the Patagonian Shelf. Cont. Shelf Res. 26 (6), 703–720.
Rivas, A.L., Pisoni, J.P., 2010. Identification, characteristics and seasonal evolution of surface thermal fronts in the Argentinean Continental Shelf. J. Mar. Syst. 79 (1-2), 134–143.
Romero, S.I., Piola, A.R., Charo, M., Garcia, C.A.E., 2006. Chlorophyll-a variability off Patagonia based on SeaWiFS data. J. Geophys. Res.: Oceans 111 (C5).
Saraceno, M., Martín, J., Moreira, D., Pisoni, J.P., Tonini, M.H., 2022. Physical changes in the Patagonian shelf. Global Change in Atlantic Coastal Patagonian Ecosystems: A Journey Through Time. Springer International Publishing, Cham, pp. 43–71.
Saraceno, M., Provost, C., Piola, A.R., Bava, J., Gagliardini, A., 2004. Brazil malvinas frontal system as seen from 9 years of advanced very high resolution radiometer data. J. Geophys. Res.: Oceans 109 (C5).
Schmit, T.J., Griffith, P., Gunshor, M.M., Daniels, J.M., Goodman, S.J., Lebair, W.J., 2017. A closer look at the ABI on the GOES-R series. Bull. Am. Meteorol. Soc. 98 (4), 681–698.
Schmit, T.J., Gunshor, M.M., Menzel, W.P., Gurka, J.J., Li, J., Bachmeier, A.S., 2005. Introducing the next-generation advanced baseline imager on GOES-R. Bull. Am. Meteorol. Soc. 86 (8), 1079–1096.
Seo, H., Subramanian, A.C., Miller, A.J., Cavanaugh, N.R., 2014. Coupled impacts of the diurnal cycle of sea surface temperature on the Madden–Julian oscillation. J. Clim. 27 (22), 8422–8443.
Stevens, B., Vali, G., Comstock, K., Wood, R., Van Zanten, M.C., Austin, P.H., Lenschow, D.H., 2005. Pockets of open cells and drizzle in marine stratocumulus. Bull. Am. Meteorol. Soc. 86 (1), 51–58.
Tonini, M.H., Palma, E.D., 2017. Tidal dynamics on the North Patagonian Argentinean gulfs. Estuar., Coast. Shelf Sci. 189, 115–130.
Tonini, M.H., Palma, E.D., Piola, A.R., 2013. A numerical study of gyres, thermal fronts and seasonal circulation in austral semi-enclosed gulfs. Cont. Shelf Res. 65, 97–110.
Valla, D., Piola, A.R., 2015. Evidence of upwelling events at the northern Patagonian shelf break. J. Geophys. Res.: Oceans 120 (11), 7635–7656.